

Dual Field Passivation Strategy for High-Performance Wide-Bandgap Perovskite Solar Cells

Xuzheng Feng, Xing Li,* Zhuoxin Li, Yufei Xue, Xianggang Chen, Xiaoxu Sun, Jixiang Tang, Shuyi Liu, Zishuo Wang, Yuhang Xie, Rui Jia, Songyuan Dai, Guoping Gao,* and Molang Cai*



Cite This: *ACS Appl. Mater. Interfaces* 2025, 17, 25883–25893



Read Online

ACCESS |

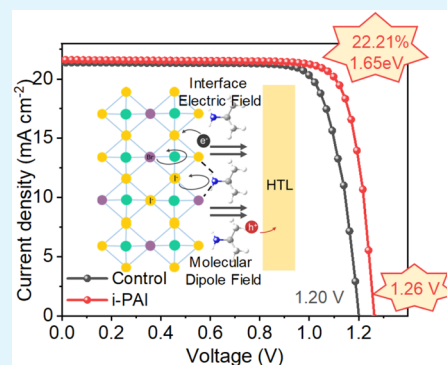
Metrics & More

Article Recommendations

Supporting Information

ABSTRACT: Wide-bandgap perovskite solar cells (WBG PSCs) have been receiving increasing focus due to the ideal application in tandem photovoltaics. Nonetheless, WBG perovskites tend to form high-density trap states, causing serious nonradiative recombination and phase segregation, which is detrimental to the efficiency and stability of WBG PSCs. In this work, a dual-field passivation strategy facilitated by isopropylamine hydroiodide (i-PAI) is introduced, in effect, showing both the molecular dipole field passivation and interface electric field passivation. This strategy reduces the charge trap density of WBG perovskite and suppresses the phase segregation, which is supported by the analysis of the experimental data and simulation results. Moreover, the dual functional passivation mitigates the open-circuit-voltage (V_{OC}) deficit of the WBG (1.65 eV) PSCs to 0.39 V and increases the efficiency to a competitive value of 22.21%. The device also exhibits excellent photostability, maintaining 84.2% of the initial efficiency after 1080 h of illumination under 1-sun white LED. This work showcases a pivotal pathway to defect passivation that can markedly enhancing both the efficiency and stability of wide-bandgap perovskite solar cells.

KEYWORDS: *dual field passivation, perovskite solar cells, phase segregation, high-performance, wide-bandgap*



INTRODUCTION

Recent progress in tandem solar cell technologies,^{1–4} has demonstrated their potential as an effective means to break through the efficiency ceiling imposed by the Shockley–Queisser limit of conventional single-junction silicon devices. Among these, the tandem structure comprising perovskite/crystalline silicon has attracted significant attention. Perovskite, as the top cell material, has been a focal point of research in the photovoltaic field due to its excellent light absorption properties,⁵ high carrier mobility,^{6–8} tunable optical bandgap,^{9,10} and simple manufacturing process.^{11,12} Based on wide-bandgap perovskite ($E_g > 1.65$ eV), perovskite/silicon tandem solar cells have achieved a record efficiency of 33.94%, representing a significant milestone in photovoltaic technology.

In general, the wide-bandgap (WBG) perovskites offer higher open-circuit voltage (V_{OC}) for the device, while they suffer from more significant voltage losses compared to conventional sub-bandgap perovskites.^{13–15} This is because WBG perovskite films tend to exhibit poor stability under illumination, as bromide and iodide ions are prone to move and recombine to form regions rich in iodine and bromine, a phenomenon known as phase segregation.^{16,17} This process generates halide vacancies and adversely affects stability. Moreover, halide ions gradually diffuse into the hole transport layer and electrodes,^{18–20} impacting device performance and ultimately deteriorating solar cell performance. During the

advancement of silicon-based solar technologies, researchers previously proposed a strategy based on field effect passivation.^{21–23} Specifically, the field-effect passivation effect generates an interfacial dipole field by inserting a dielectric film, which repels and separates free charges at the interface, preventing the formation of recombination regions. Some researchers have applied field-effect passivation to high-efficiency perovskite solar cells.^{26,27} They deposit the passivation material between PSK and the electron transport layer. The formed space electric field suppresses the recombination of holes and promotes the extraction of electrons.²⁸ However, at the same time, this electric field will cause the migration of halide ions to the electron transport layer, which may lead to worse phase stability. When an appropriate field-effect passivation material is applied to an n-i-p perovskite solar cell (PSC) and the electric field formed between PSK/HTL is in the same direction as the migration direction of halide anions, it can not only improve the extraction of holes, but also achieve the suppression of phase

Received: November 20, 2024

Revised: April 7, 2025

Accepted: April 14, 2025

Published: April 21, 2025



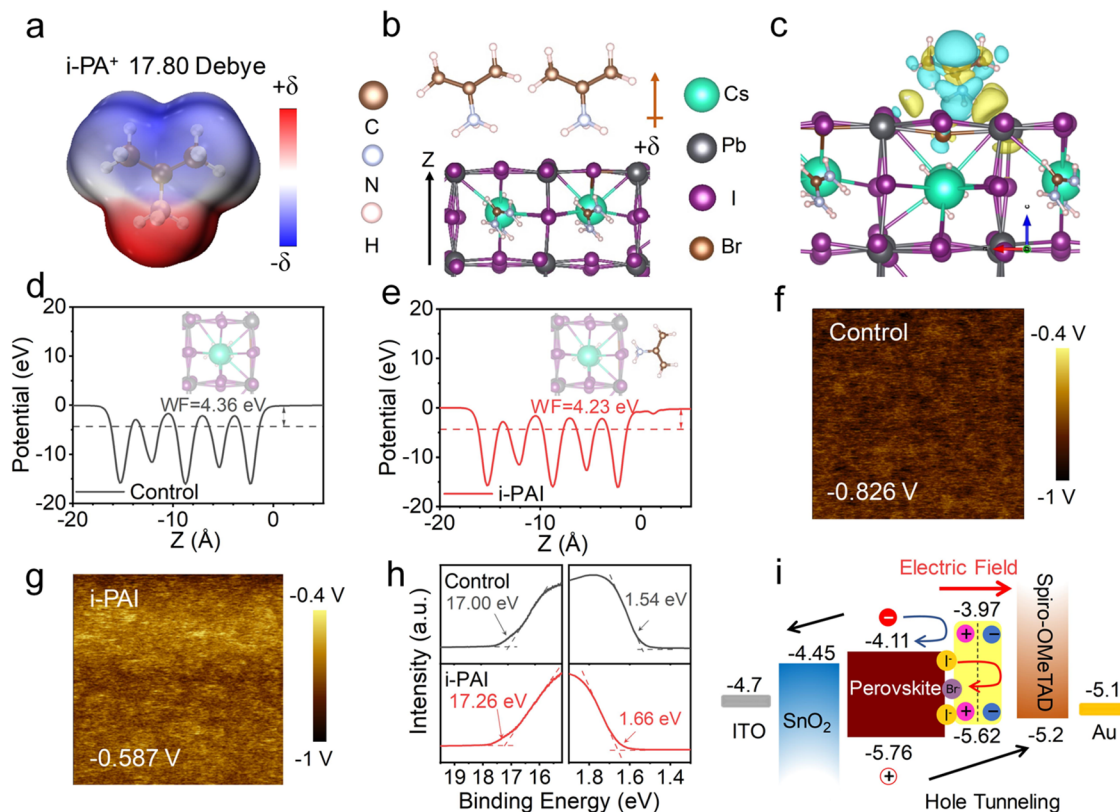


Figure 1. (a) Electrostatic potential (ESP) map of $i\text{-PA}^+$; (b) structural diagram of $i\text{-PA}^+$ cation ordering on the surface of the perovskite lattice; (c) electron density differences for the $i\text{-PA}^+$ ions on the surfaces of perovskite; plane-averaged electrostatic potential of the (d) control perovskite film (e) perovskite film treated by $i\text{-PAI}$ along the z axis; KPFM images of the (f) control and (g) perovskite film after treatment with $i\text{-PAI}$; (h) comparative UPS spectra between control and $i\text{-PAI}$ -treated perovskite films; (i) device energy level diagram.

segregation. The contact between the passivation agent and the perovskite's top interface unavoidably results in charge redistribution, which in turn induces an interfacial field effect. In combination with the molecular dipole field effect mentioned previously, this results in a dual field passivation strategy. This strategy, which has been scarcely reported, effectively reduces the trap density of WBG perovskites and suppresses phase separation, ultimately enhancing the performance of mixed-halide WBG PSCs.

Here, we introduce the isopropylamine hydroiodide ($i\text{-PAI}$) as an interfacial modifier between mixed-halide WBG perovskite and spiro-OMeTAD layers. The highly polar ammonium salt establishes a stable molecular dipole field, which, in conjunction with the interfacial electric field induced by charge exchange between $i\text{-PAI}$ and the perovskite, contributes to a synergistic passivation effect. The migration of halide ions toward the perovskite film surface and into the spiro-OMeTAD layer is restricted, reducing defects and thereby suppressing phase separation. Through the dual field passivation strategy achieved using $i\text{-PAI}$, the maximum PCE of the improved n-i-p device can reach 22.21% ($V_{OC} = 1.263$ V, fill factor (FF) = 81.35%), short-circuit current density ($J_{SC} = 21.62$ mA cm⁻²). The $i\text{-PAI}$ -treated device shows only 15.8% efficiency degradation after 1080 h in 15–20% RH environments.

RESULTS AND DISCUSSION

Since $i\text{-PAI}$ with amino groups (The molecular Ball-and-Stick model is shown in Figure S1) may establish a dipole-based passivation coating on the perovskite surface, the WBG

perovskite film was treated by spin-coating with a 10 mM $i\text{-PAI}$ solution in isopropanol (see detailed description in SI) to introduce a passivation layer.

To enhance the comprehension of this passivation material, the electrostatic potential characteristics of the $i\text{-PA}^+$ state were investigated through simulations utilizing density functional theory (DFT), the calculated results reveal a dipole moment of 17.80 D, indicating a strong polarity of the $i\text{-PA}^+$ ion. This strong molecular polarity arises from the more directional distribution of electron clouds around the $i\text{-PA}^+$ ion, leading to an uneven charge distribution, as shown in Figure 1a, which form an electric field on the perovskite film.

For the purpose of elucidating the molecular dipole orientation resulting from $i\text{-PAI}$ surface treatment, the relative position of the $i\text{-PA}^+$ ion upon contact with the mixed-halide perovskite film was discovered by additional investigation of the interaction at the interface of the $i\text{-PA}^+$ cation and the perovskite layer. This information was derived from DFT calculations and is displayed in Figure 1b. It can be observed that the amino side of the $i\text{-PA}^+$ ion, which carries a positive charge (see Figure 1a), points toward the perovskite film, indicating that the direction of the molecular dipole electric field formed by it is from the perovskite film toward the hole transport layer. Furthermore, the electron density difference calculations were performed to analyze the charge transfer process triggered by the contact of $i\text{-PA}^+$ ions with the perovskite film. The turquoise and yellow regions shown in Figure 1c represent charge depletion and accumulation, respectively. The results indicate that a significant amount of charge from the $i\text{-PA}^+$ ions is transferred to the perovskite film.

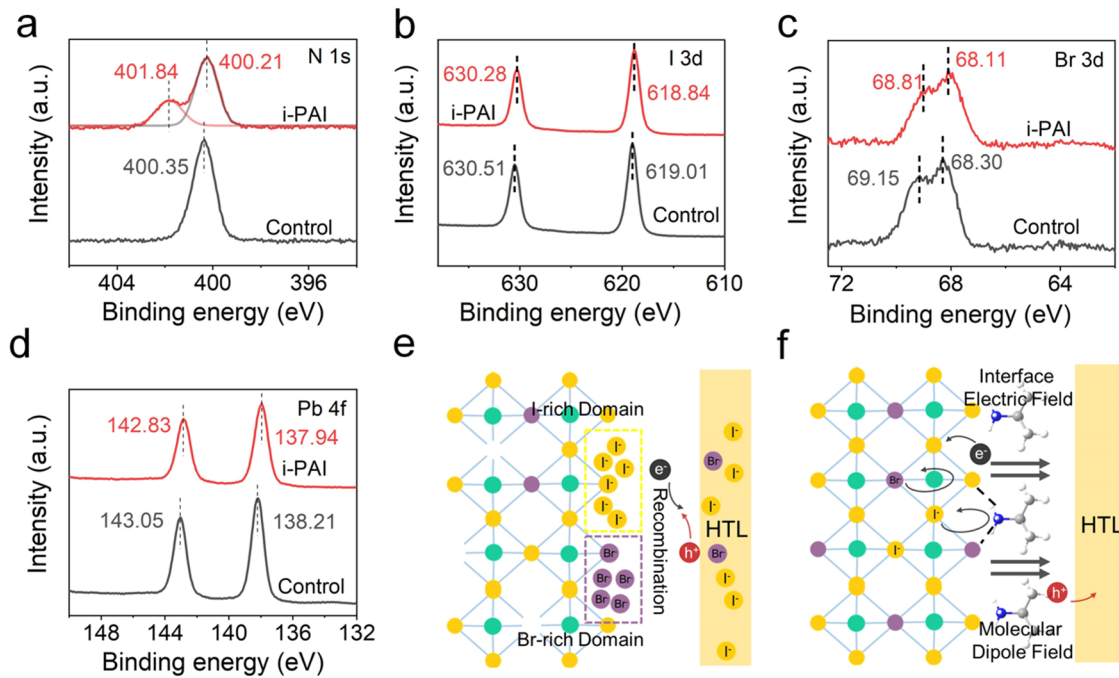


Figure 2. XPS spectra of (a) N 1s (b) I 3d (c) Br 3d and (d) Pb 4f elements for the control and i-PAI-treated perovskite film. Schematic of (e) control perovskite surface and (f) the dual field passivation mechanism.

This charge transfer creates an interface electric field within the perovskite's near-surface region that opposes the direction of the transferred charge and aligns with the molecular dipole field direction. The combined action of the dual fields effectively restrains the outward diffusion of halide ions from the perovskite layer, thereby mitigating phase segregation and simultaneously promoting hole extraction and mobility. This passivation approach, combining the effects of molecular dipole field passivation and interface electric field passivation, is referred to as the dual field passivation strategy.

Under the influence of dual field passivation, the electronic states at the surface of the perovskite film are bound to undergo significant alterations. KPFM measurements were performed to characterize the i-PAI-modified perovskite surface potential.²⁹ As shown in Figure 1f,g, the introduced i-PAI altered the surface potential of the perovskite film. The average electric potential in the test area changes from -0.826 to -0.587 V.

Based on the provided equation

$$\text{CPD} = (\text{WF}_{\text{tip}} - \text{WF}_{\text{sample}})/e \quad (1)$$

Where e represents the basic electronic charge, WF_{tip} denotes the tip work function (WF), and $\text{WF}_{\text{sample}}$ corresponds to the sample work function. The decline in CPD is indicative of an upward shift in the sample's work function. Therefore, surface treatment with i-PAI can alter the work function of WBG perovskite films, which is closely related to the formation of the electric field generated by i-PAI on the surface of the perovskite film.

Considering that the passivation agent has already made significant changes to the surface electrical properties of the perovskite film, we intend to assess the effects of these additives on the morphology of the perovskite film through atomic force microscopy (AFM) and scanning electron microscopy (SEM) evaluations, according to Figures S2 and S3. According to the AFM test results, the perovskite layer

treated with i-PAI exhibits a smaller root-mean-square (RMS) surface roughness of 19.8 nm, while the untreated perovskite layer has an RMS of 29.3 nm. Additionally, a 1 μm -long profile across the grain boundary was selected from the AFM images to study the distribution of i-PAI on the surface of the perovskite film, as depicted in Figure S2c,d. The surface of the i-PAI treated perovskite film (33.02 nm) displayed more pronounced "peak-valley" features relative to the control film (52.25 nm). The results demonstrate that i-PAI preferentially deposits within perovskite grain boundary domains, leading to a reduction in the overall roughness of the perovskite film. A smoother surface is a key advantage in achieving close interface contact, effectively suppresses current leakage pathways by increasing shunt resistance. A comparison of the SEM images of the untreated and i-PAI treated perovskite films shows that the average grain size of the untreated film is around 348.84 nm, while the treated film exhibits a marginally larger average grain size of 357.86 nm. It was observed that the surface morphology of perovskite films was not significantly changed after the passivation treatment of i-PAI. Plane-averaged electrostatic potential calculations were employed to evaluate the work function profile along the surface-normal direction, as shown in Figure 1d,1e. The results indicate that, after contact with i-PAI⁺ ions, the work function of the perovskite film changes from 4.36 to 4.23 eV, which aligns well with the trend observed in the experimental results. This suggests that the aligned dipole configuration effectively modifies the surface energy landscape and increases the potential difference. To further characterize the band-edge energy of the perovskite film under the dual field passivation strategy, ultraviolet photoelectron spectroscopy (UPS) was performed,^{30,31} with the results presented in Figure 1h. Compared to the control film, the i-PAI-treated perovskite film exhibits a lower work function, which aligns with the results from KPFM and simulations, confirming our hypothesis. Combined with the bandgap shown in Figure S4 and the test results of ultraviolet

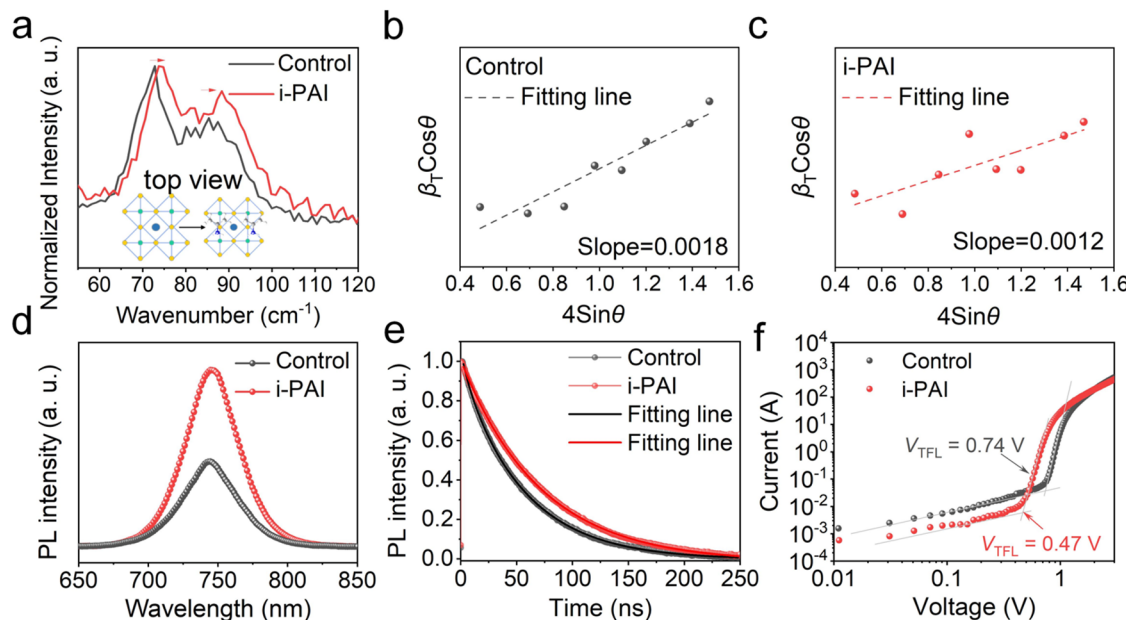


Figure 3. (a) Raman spectra of PbI_2 film and film doped with i-PAI using a 532 nm laser source. W–H analysis of crystal strain in (b) unmodified versus (c) i-PAI-passivated perovskite, (d) steady-state PL spectra, (e) normalized TRPL spectra of the perovskite film without and with i-PAI treated. (f) dark J – V curves for the fabricated single-carrier devices.

photoelectron spectroscopy, the energy level structure schematic diagram as shown in Figure 1*i* can be obtained. It is observed that subsequent to the surface treatment with iPAI, both the valence band maximum (E_V) and conduction band minimum (E_C) of the perovskite surface exhibit a shift toward the vacuum level, resulting in a more compatible energy band structure. This finding implies that such treatment accomplishes field effect passivation and mitigates interface recombination.

To achieve a deeper insight into the interface electric field effect between i-PAI and the components within the perovskite, X-ray photoelectron spectroscopy (XPS) was utilized. Through comprehensive analysis of the XPS data both prior to and following surface treatment, the elemental composition, along with the electronic and chemical states of the constituent elements, can be accurately identified. In the results shown in Figure 2*a*, for the perovskite with i-PAI treatment, we found that a peak emerges at a binding energy of 401.84 eV, consistent with ammonium group of the i-PA^+ cations, confirming the existence of i-PAI on perovskite, and also In addition to the characteristic N 1s peaks, the modified sample exhibits a 0.14 eV negative shift relative to the control's 400.35 eV position, now centered at 400.21 eV. As shown in the XPS results in Figure 2*b,c*, the interactions between i-PAI and the halide ions in the perovskite has been identified.³² After treatment, the Br 3d characteristic peaks of the control perovskite film are at 69.15 eV (Br 3d 3/2) and 68.30 eV (Br 3d 5/2), which experience a systematic binding energy downshift upon i-PAI functionalization (68.81 eV, 68.11 eV). Similarly, the I 3d characteristic peaks of the control perovskite film, initially observed in Figure 2*b* at 630.51 eV (I 3d 3/2) and 619.01 eV (I 3d 5/2), shift to lower binding energy values of 630.28 and 618.84 eV with i-PAI treatment, respectively. As indicated in Figure 2*d*, the Pb 4f peaks of the control perovskite film, originally at 143.05 eV (Pb 4f 5/2) and 138.21 eV (Pb 4f 7/2), shift to lower binding energies of 142.83 and 137.94 eV upon i-PAI treatment.

According to fundamental photoelectron spectroscopy principles, the electron binding energy (E_B) can be determined by the equation $E_B = h\nu - E_K - \text{WF}$, where $h\nu$ represents the photon energy, E_K denotes the measured kinetic energy. E_B is characteristically different for atoms with various electronic shells.³³ To a certain extent, it also depends on the chemical environment of the atom. In other words, variations in chemical coordination environments manifest as characteristic shifts in photoelectron kinetic energies. Increased electron density at an atomic site raises the kinetic energy (E_K) of emitted core-level photoelectrons, consequently reducing the observed binding energy (E_B) shift in the spectrum. Given that the peak positions of I, Br, and Pb all shift in the direction of a lower binding energy, it is demonstrated that the electron density on the atoms of these three elements is heightened, aligning with the simulation results that following the adsorption of i-PAI onto the surface of the perovskite film, a transfer of 0.14 electrons to the perovskite occurs. Moreover, this observation further supports the existence of an interface electric field, aligned with the direction of the dipole field, arising from charge transfer that takes place after the adsorption of i-PAI on the perovskite film surface, which is named as interface electric field passivation.

This observation also indicates that the application of i-PAI surface treatment leads to significant coupling interactions between the $-\text{NH}_4^+$ nitrogen element in the i-PA^+ ion, halide ions, and Pb_2^+ in the perovskite film, allowing the i-PA^+ ions to firmly adhere to the surface of the perovskite film and making it difficult for them to migrate laterally at the interface. This is significant for inhibiting the phase separation of mixed-halide WBG perovskite materials. Therefore, by being applied to the surface of the perovskite film, i-PA^+ ions can also effectively passivate defects in the perovskite film.

To explore how the dual field passivation strategy formation process impacts ion distribution, time-of-flight secondary ion mass spectrometry (ToF-SIMS) analysis was used in a detailed manner. As shown in the depth profiling data presented in

Figure S5, signals for both Br^- and I^- ions were detectable within the sputtering depth range. Notably, no significant accumulation of these ions was observed in the near-surface region, where the distribution remained relatively uniform. These findings indicate that the construction of the electric field does not induce ion migration, and thus, no ion enrichment occurs on the surface. Under typical conditions, the phenomenon of photoinduced phase separation in mixed-halide wide-bandgap perovskite layers leads to halide ion migration toward the hole transport layer. This migration can subsequently result in chemical reactions between halide ion and the silver electrode, causing electrode corrosion, which significantly impacts the device's performance and operational stability. However, under dual field passivation, the diffusion of halide anions from the perovskite film surface to the hole transport layer is effectively suppressed. **Figure S6** vividly illustrates the conditions of the silver electrode on the side of complete devices after 480 h of continuous illumination in a nitrogen atmosphere, comparing a control group with devices treated using i-PAI. In the control device, the silver electrode exhibits severe corrosion, whereas the silver electrode in the i-PAI-treated device remains in a well-preserved state. This observation highlights the effectiveness of i-PAI treatment in mitigating halide migration and protecting the electrode from degradation under operational conditions.

Under the synergistic action of dipole electric field and interface electric field effect, the application of field effect passivation on the upper interface of n-i-p perovskite solar cells can yield outstanding passivation effects. The passivation mechanism is illustrated in **Figure 2e,f**. This depiction provides a visual representation of the intricate processes involved in the passivation mechanism, offering valuable insights into the underlying principles and enhancing our understanding of the effectiveness of dual field passivation in n-i-p perovskite solar cells.

Along with generating both a dipole and interfacial electric field on the perovskite film's surface, i-PAI plays a key role in modifying the fundamental properties of the perovskite film. To investigate the interaction mechanism between i-PAI and PbI_2 , i-PAI was doped into the PbI_2 precursor solution, followed by Raman spectroscopy measurements, with the data normalized accordingly. As illustrated in **Figure 3a**, the results indicate a blue shift in the Raman diffraction peaks of PbI_2 toward higher wavenumbers, signifying that the interaction between i-PAI and PbI_2 induces compressive strain in the lattice, leading to lattice contraction. This phenomenon is consistent with the trend in Pb—I bond length changes on control and treated perovskite films, as statistically derived from the simulation results presented in **Table 1**. Subsequently, Raman spectroscopy was performed on PbI_2 films subjected to ultraviolet (UV) light aging. As shown in **Figure S7**, the control group's films exhibit a shift of the PbI_2 Raman diffraction peaks to lower wavenumbers after light aging, indicating that the

lattice undergoes tensile strain and expansion. In contrast, the Raman diffraction peaks of PbI_2 films doped with i-PAI exhibit minimal shifts, demonstrating a more stable lattice structure, thereby corroborating the aforementioned observations. As depicted in **Figure S8a**, X-ray diffraction (XRD) measurements revealed that perovskite films treated with i-PAI did not exhibit any diffraction peaks associated with low-dimensional perovskite, nor did the crystal orientation of the perovskite undergo any changes. To further elucidate the mechanical properties of the perovskite films influenced by i-PAI, The Williamson—Hall (W—H) method, depicted in **Figure 3b,3c**, was applied to assess the microstrain in the control and i-PAI-treated perovskite films. The slopes of the W—H fitting curves for the control and i-PAI-treated films were estimated to be 0.0018 and 0.0012, correspondingly, indicating that i-PAI effectively reduces the strain in perovskite films deposited on glass/ SnO_2 substrates.³⁴ Consistent with this observation, density functional theory (DFT) calculations, as summarized in **Table 1**, demonstrate that the introduction of i-PAI reduces the average I—Pb—I bond angle from 93.05 to 91.98°, bringing it closer to 90°, indicating reduced deformation of the perovskite cubic lattice. This reduction in strain is in agreement with the results obtained via the Williamson-Hall method. The schematic illustration of the lattice structural changes is presented in **Figure S8b**.

Figure 3d demonstrates that the perovskite film, after surface passivation, exhibits a significant enhancement in photoluminescence (PL) intensity, implying a notable decrease in nonradiative recombination losses, which demonstrates the effective passivation of defects by i-PAI.³⁵ We used a double-exponential function to fit the decay curve of time-resolved photoluminescence (TRPL), and the fitting curve is shown in **Figure 3e**.

$$I(t) = A_1 \exp(-t/\tau_1) + A_2 \exp(-t/\tau_2) \quad (2)$$

The decay process of TRPL involves two stages: fast decay and slow decay, where the former is typically ascribed to the quenching effect of defects in perovskite layer, while the latter is caused by the free carrier recombination. Here, τ_1 and τ_2 represent the nonradiative (fast) and radiative (slow) recombination pathways, correspondingly, and the average lifetime (τ_{avg}) can be calculated as $\tau_{\text{avg}} = A_1\tau_1 + A_2\tau_2$. The computational data indicate that the carrier lifetime of the control perovskite film is 53.48 ns. In contrast, the perovskite film treated with i-PAI exhibits a longer carrier lifetime, with a τ_{avg} value of 70.76 ns. Therefore, the improvement of photoluminescence intensity and lifetime shows that the surface modification of i-PAI can effectively passivate the nonradiative recombination defects.^{36,37} We also conducted an analysis of the Urbach energy (E_u) for the devices before and after surface treatment. The Urbach energy is a key parameter used to describe the density of defect states in the tail of the bandgap. A lower E_u value typically indicates a reduced defect density within the material, which correlates with smaller carrier recombination losses. In **Figure S9**, the E_u value for the untreated device was found to be 53.31 meV, whereas for the device after i-PAI surface treatment, the E_u value was reduced to 34.91 meV, suggesting that the surface treatment effectively lowered the defect density in the perovskite film, thereby improving charge transport efficiency and reducing carrier recombination losses. Furthermore, comparative space-charge-limited current (SCLC) measurements of electron-only devices (ITO/ SnO_2 /perovskite/ C_{60} /Ag) show V_{TFL} lowering

Table 1. Statistics of the Lengths and Angles of I—Pb—I and Bonds in the Perovskite Lattice before and after the Introduction of i-PAI

I—Pb—I	bond angle (°)	bond length (Å)
control	93.05	3.56
i-PAI	91.98	3.31
difference	-1.07	-0.25

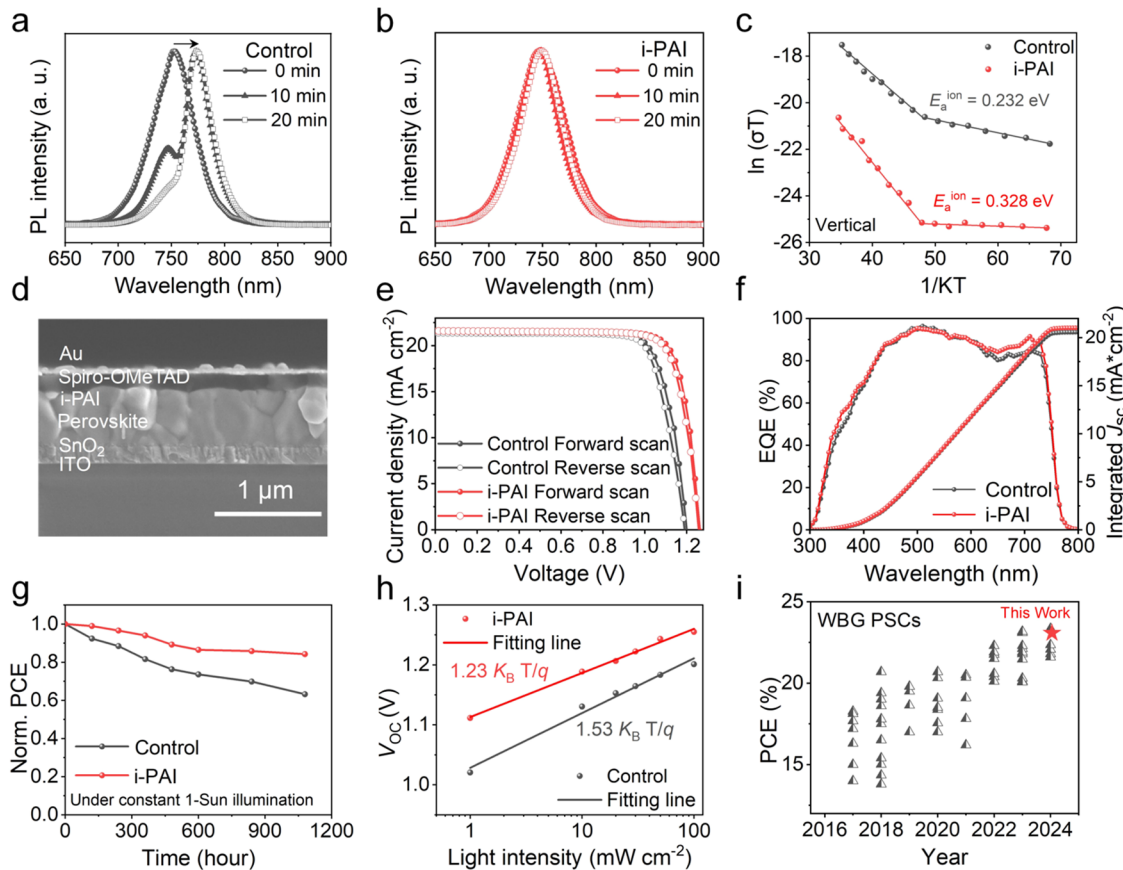


Figure 4. PL spectra of the (a) control film and (b) i-PAI treated film under 365 nm UV light for 20 min. (c) Temperature-dependent conductivity measurements in the vertical direction for both control and i-PAI-treated perovskite films. (d) Cross-sectional electron microscopy of n-i-p WBG PSCs. (e) J – V curves measured under both forward and reverse scanning directions, (f) EQE spectra of the devices without and with i-PAI. (g) Photostability characterization of packaged devices under simulated 1-sun conditions (white LED source) (h) Dependency of V_{OC} on the light intensity for the devices based on the control and i-PAI treated perovskite films. (i) The PCE of the state-of-the-art WBG PSCs with different bandgaps.

from 0.74 to 0.47 V, demonstrating trap density suppression by a factor of i-PAI through surface treatment shown in Figure 3f for the devices fabricated in the two condition, correspondingly. Based on the trap-filled limit regime in SCLC measurements, the defect density was calculated using V_{TFL} according to

$$N_t = \frac{2\epsilon_r \epsilon_0 V_{TFL}}{qL^2} \quad (3)$$

Where ϵ_r is the relative dielectric constant of the perovskite semiconductor, ϵ_0 denotes the fundamental vacuum permittivity constant, q represents the elementary charge, and L corresponds to the perovskite layer thickness. V_{TFL} marks the voltage required to fill all trap states in the bandgap obtained from the J – V curve. Consequently, the trap concentration is remarkably suppressed by nearly 1 order of magnitude, decreasing from $8.35 \times 10^{15} \text{ cm}^{-3}$ to $5.19 \times 10^{15} \text{ cm}^{-3}$, implying a reduction in the defect density of the treated perovskite film,^{38,39} consistent with the results of PL and TRPL tests. To quantitatively assess nonradiative recombination losses, the external quantum efficiency of electroluminescence (EQE_{EL}) was characterized via driving the photovoltaic device in light-emitting diode mode under forward bias conditions. As shown in Figure S10, we selected an EQE_{EL} of 0.15% and observed a significantly higher EQE_{EL} of 1.7% corresponding to the device treated with i-PAI at a

photogenerated current density of 27.94 mA/cm². In light of these findings, the nonradiative recombination losses ($\Delta V_{OC,\text{nonrad}}$) being of assistance to the total V_{OC} loss were determined using the following relationship

$$\Delta V_{OC}^{\text{nonrad}} = \frac{k_B T}{q} \ln \text{EQE}_{EL}^{-1} \quad (4)$$

Where k_B represents the Boltzmann constant, q corresponds the elementary charge, T denotes the ambient temperature. Based on the analysis $\Delta V_{OC,\text{nonrad}}$ for the untreated and i-PAI-treated devices are 0.16 and 0.10 V, correspondingly. This systematic variation in $\Delta V_{OC,\text{nonrad}}$ between devices with different post treatment is consistent with the distinction in V_{OC} , indicating that the enhancement in V_{OC} through i-PAI chemical passivation is mainly attributed to the reduction in nonradiative recombination losses. Therefore, the comprehensive results above confirm that the introduction of i-PAI between the perovskite and hole transport layer effectively suppresses nonradiative recombination, thereby enhancing the V_{OC} and PCE.

Comparative UV–visible (UV–vis) absorption spectra presented in Figure S4 reveal distinct optical transitions between control and i-PAI-modified perovskite films. Compared to the reference film, the perovskite film treated with i-PAI exhibits a notable increase in absorption intensity within the visible light region. The results demonstrate the change in

$(A\hbar\nu)^2$ versus $\hbar\nu$ obtained from the absorption spectra of perovskite samples with and without passivation treatment, using the Tauc plot method.⁴⁰ The findings reveal that the optical bandgap of the perovskite film stays the same after i-PAI treatment, with both films having a bandgap close to 1.65 eV.

Given the susceptibility of I/Br mixed-halide perovskites to halide segregation often referred to as photoinduced phase segregation or the Kirkwood effect—the photostability under illumination serves as a critical indicator of the stability of mixed-halide WBG perovskites. To evaluate the impact of the dual field passivation effect of i-PAI on the phase stability of mixed-halide perovskites, we conducted steady-state photoluminescence (PL) measurements on the perovskites in operational stability testing (continuous 365 nm UV exposure, ambient conditions) irradiation for 20 min and normalized the results. As depicted in Figure 4a, a gradual redshift of the main peak and the emergence of a shoulder peak at lower wavelengths were observed in the control group films with increasing light exposure time, indicating phase segregation with the formation of a narrow-bandgap I rich phase and a WBG Br rich phase. In contrast, the PL peak morphology of the i-PAI-treated films remained largely unchanged after 20 min of UV irradiation which is shown in Figure 4b. We plotted the PL peak position maps to study the effect of i-PAI on the perovskite films' stability when illuminated. As observed in Figure S11, the control films display a markedly poor uniformity in the PL peak position distribution after exposure to UV light, signaling notable photoinduced phase segregation. In contrast, the original condition of the WBG perovskite treated by i-PAI and the PL peak position mapping after 10 and 20 min of UV light exposure, demonstrating remarkable photostability after light-aging time. The increased active migration energy was validated by experimental measurements through capturing the vertical temperature dependent conductivity of the normal and target films. The ion active migration energy in the treated film was 0.328 eV, which was larger than the control film's (0.232 eV) displayed in Figure 4c, fundamentally indicating that the surface treatment with i-PAI can effectively suppress ion migration and phase separation, a phenomenon attributed to the robust dual field passivation strategy employed. To investigate the influence of molecular dipole field passivation and interfacial electric field passivation on the horizontal phase separation of perovskite films, we performed temperature-dependent conductivity measurements along the horizontal direction. By contrasting the temperature-dependent conductivity of the reference film and the passivated film, the experiments validated the increase in activation energy for ion migration. The activation migration energy of the treated films was found to be 0.413 eV, which is higher than the 0.367 eV observed for the control films in Figure S12. This fundamentally indicates that the surface treatment with i-PAI not only effectively suppresses ion migration and phase separation in the vertical direction but also exerts a significant inhibitory effect on phase separation in the horizontal direction. The increase in activation energy for ion migration in the horizontal direction was 0.046 eV, which is relatively smaller than the 0.096 eV increase observed in the vertical direction, as shown in Figure R11c. This indicates that the dual field passivation strategy is more effective in suppressing ion migration in the vertical direction compared to the chemical passivation effect in the horizontal direction. Since ion migration typically occurs at the grain boundaries,

the introduction of dual field passivation plays a crucial role in inhibiting ion migration between perovskite and HTL, which is essential for improving the performance of wide-bandgap perovskite solar cell devices.

To minimize the potential influence of the reduction of defects and the alleviation of strain on the suppression of phase separation, a reference surface passivation material, GAI, was selected for comparison with i-PAI, as shown in Figure S13a. Based on DFT calculations, it was found that the GA^+ ion, which possesses a relatively high structural symmetry, has a negligible dipole moment of 1.89 D, which is significantly lower than that of the i- PA^+ ion (17.80 D), and thus GA^+ can only generate a relatively weaker molecular dipole field passivation effect. As depicted in Figure S13b,c, both PL and SCLC tests demonstrated that GAI surface treatment can effectively improve the quality of the films and reduce defects. Furthermore, XRD measurements and W–H fitting analysis, shown in Figure S13d,e, indicate that this process also contributes to the reduction of film stress. Building upon this, as can be observed from the photoluminescence (PL) spectrum in Figure S13f, phase separation still occurred in the GAI treated films, indicating that the high phase stability achieved through the dual field passivation strategy employed in this work is particularly momentous.

In the application of i-PAI surface treatment for mixed-halide WBG PSCs, the concentration of i-PAI was optimized. Statistical performance data for devices with different i-PAI concentrations, including the control group, is shown in Figure S14. The analysis reveals that the device treated with a 10 mM i-PAI solution exhibits significantly improved performance, highlighting the importance of optimizing surface treatment concentration for better device efficiency. Then, to look into how i-PAI affects the photovoltaic performance of perovskite solar cells, we fabricated glass/indium-doped tin oxide (ITO)/tin oxide (SnO_2)/WBG perovskite/(i-PAI) spiro-OMeTAD/gold (Au) perovskite solar cells based on the formal structure. Figure 4d shows the cross-sectional scanning electron microscope images of the device. Figure 4e displays the forward and reverse scan current density–voltage (J – V) curves of the reference device and the WBG PSCs passivated with i-PAI. Table 2 comprehensively presents the device photovoltaic

Table 2. Photovoltaic Performance Metrics of the Highest-Efficiency Wide-Bandgap Perovskite Solar Cells

sample		J_{SC} [mA cm^{-2}]	V_{OC} [V]	FF [%]	PCE [%]
control	forward	21.39	1.201	79.11	20.32
	reverse	21.33	1.192	78.6	19.98
i-PAI	forward	21.62	1.263	81.35	22.21
	reverse	21.60	1.258	80.31	21.82

characteristics under standard test conditions (AM 1.5G, 25 °C, 100 mW/cm²). The PCE of the untreated control device is 20.32%, with a V_{OC} of 1.20 V, J_{SC} of 21.39 mA cm⁻², and FF of 79.11%. The photovoltaic performance of the solar cell device modified by i-PAI is slightly improved, with a PCE of 22.21%, V_{OC} of 1.263 V, comparable to traditional iodine-based perovskite systems, J_{SC} of 21.62 mA/cm², and FF of 81.35%. This indicates that the modified WBG perovskite devices have better energy level alignment and defect modification, promoting the increase in V_{OC} , J_{SC} and FF. As evidenced in Figure 4i, our WBG-PSC achieves a high certified efficiency ranking among the highest reported values in literature. A

performance comparison was conducted between the solar cell fabricated in this work and state-of-the-art devices with similar bandgaps shown in **Table S1**. The n-i-p device fabricated herein, achieving a remarkable power conversion efficiency of 22.21% at a bandgap of 1.65 eV, demonstrated outstanding performance characterized by exceptionally low voltage losses. The corresponding steady-state power output measurements of the control devices and the devices with i-PAI surface treatment are presented in **Figure S15**. Steady-state photocurrent measurements at 1.08 V demonstrate exceptional operational stability in treated devices, the current density and power conversion efficiency show no significant change within 400 s, among which the stabilized power conversion efficiency is 21.79%. These results underscore the improved reliability and performance of wide-bandgap perovskite solar cells achieved through surface treatment, highlighting its efficacy in addressing stability challenges inherent to such devices. **Figure 4f** shows the measured EQE. The integrated photocurrent of the best device is 21.53 mA cm⁻², consistent with the short-circuit current derived using the *J*–*V* curve. **Figure S16** presents the PCE performance of the devices before and after passivation. Compared to the untreated devices with a PCE of 18.18% ± 0.96%, the average PCE of the devices treated with i-PAI is significantly improved to 20.33% ± 0.78%, with significantly improved repeatability. Particularly noteworthy is that the maximum *V*_{OC} has reached 1.263 V, achieving a lower *V*_{OC} deficit of 0.387 V, comparable to traditional iodine-based perovskite systems. Stability evaluation was conducted under 1 sun equivalent white LED light illumination in a nitrogen atmosphere. As shown in **Figure 4g**, after 1080 h, the device treated with i-PAI maintained 84.2% of the initial PCE, while the untreated device experienced a significant decline, maintaining only 63.2% of the initial PCE. This observation suggests that the additive markedly enhances the light stability of perovskite solar cells, attributable to the synergistic effect arising from the superior molecular dipole field passivation and the interface electric field passivation capabilities conferred by i-PAI.

Moreover, the dependence of device *V*_{OC} on light intensity was explored in **Figure 4h**. According to the formula

$$V_{OC} = (nk_B T/q) \ln(I/I_0 + 1) \quad (5)$$

Where *k*_B represents the Boltzmann constant, *T* corresponds the temperature, and *n* donates the ideal factor.⁴¹ The computed *n* values were 1.53 and 1.23, for control device and i-PAI treated device respectively, representing the lower Shockley–Read–Hall (SRH) recombination.

The improvement in *V*_{OC} due to i-PAI treatment was further corroborated by Mott–Schottky analysis, as shown in **Figure S17**, where the built-in potential (*V*_{bi}) can be extracted from the intercept of the Mott–Schottky plot. As depicted, the *V*_{bi} increased from 1.05 to 1.08 V following the i-PAI surface treatment. The increased built-in field facilitates the separation of photogenerated electron–hole pairs and enhances carrier collection, thus mitigating voltage losses in the solar cell. The charge recombination dynamics of the WBG perovskite devices in the dark condition were studied by electrochemical impedance spectroscopy (EIS). Compared with the control device, the i-PAI treated device was enlarged shown in **Figure S18**, indicating that the i-PAI could effectively increase the charge recombination resistance, promote the transfer of charges, and mitigate the nonradiative recombination,⁴² resulting in a higher *V*_{OC}.

CONCLUSIONS

An efficient and stable wide-bandgap perovskite solar cell was realized through a dual field passivation strategy, where i-PAI, characterized by its strong dipole moment and amino functionalities, was employed to modify the 1.65 eV perovskite surface. Through its significant dipole moment, i-PAI establishes a directionally aligned molecular dipole electric field between the perovskite layer and the spiro-OMeTAD layer. In conjunction with the interface electric field generated by charge exchange, this effectively inhibits the diffusion of halide ions from the mixed halide perovskite to the hole transport layer, thereby minimizing the migration of halide ions within the perovskite film and ultimately suppressing phase separation. Furthermore, this surface passivation enhances the extraction of charge carriers by the hole transport layer and improves energy level alignment, significantly increasing the open-circuit voltage, fill factor, and stability of the n-i-p type mixed halide WBG PSCs. Finally, we fabricated the high-performance mixed-halide perovskite solar cells (*E*_g = 1.65 eV), achieving a *V*_{OC} of 1.263 V and a maximum device efficiency of 22.21%. This study provides a promising interface modification approach for efficient and stable mixed-halide WBG PSCs, combining field and chemical passivation strategies, which could contribute to the advancement of photovoltaic technology based on perovskite materials.

EXPERIMENTAL SECTION

Materials. All precursor materials were acquired from commercial suppliers and used without further purification. Specifically, high-purity halide salts including PbI₂ (99.99%), PbBr₂ (99.99%) from TCI, and CsI (99.9%) from Aladdin were obtained. Organic components consisted of FAI (GreatCell Solar Ltd, 99.8%) and the hole-transport material Spiro-OMeTAD (Xi'an Polymer Light Technology Corp). Additives such as tBP and Li-TFSI were sourced from Innochem, while the SnO₂ was procured from Alfa Aesar. Anhydrous solvents (DMF, DMSO, IPA, CB) with guaranteed purity were supplied by Alfa Aesar. Commercial patterned ITO/glass substrates (15 Ω cm⁻¹) were used as received from Xinyan Technology Ltd.

Device Fabrication. The wide-bandgap perovskite solar cells adopted a planar heterojunction configuration with the layer sequence: glass/ITO/SnO₂/perovskite/Spiro-OMeTAD/Au. Laser-patterned ITO/glass substrates (Rs ≤ 15 Ω/sq, thickness: 135 nm) were subjected to a rigorous cleaning protocol consisting of: (1) detergent sonication, (2) sequential rinsing with deionized water (2 cycles), (3) acetone degreasing, and (4) ethanol purification (2 cycles) prior to device fabrication. Subsequently, it was subjected to UV ozone exposure for 15 min. An aqueous SnO₂ colloidal solution (2.6 wt %) was deposited on the precleaned ITO substrates via spin-coating (5000 rpm, 30 s), followed by thermal annealing at 150 °C for 30 min under ambient conditions. The Cs_{0.1}FA_{0.8}MA_{0.1}Pb(I_{0.78}Br_{0.22})₃ precursor comprised PbI₂, PbBr₂, CsI₂, FAI and MAI in DMF/DMSO (4:1 v/v) with overnight agitation. The device fabrication process involved sequential deposition steps: Perovskite precursor solution (50 μL) was spin-coated on SnO₂ substrates (3500 rpm, 40 s; acceleration: 500 rpm/s) with chlorobenzene antisolvent dripping (120 μL), followed by thermal annealing (150 °C, 20 min). Surface passivation was achieved by spin-coating 10 mM i-PAI/IPA solution (50 μL) and subsequent heating (100 °C, 10 min). The hole transport layer was formed by depositing Spiro-OMeTAD solution at 3500 rpm for 30 s. Finally Au electrodes (80 nm) were thermally evaporated.

Characterizations. Time-of-flight secondary ion mass spectrometry (TOF-SIMS) analysis was performed using an IONTOF TOF-SIMS 5–100 instrument with dual-beam configuration: (i) Bi₃⁺ primary ion beam (30 kV, 45° incidence) for surface analysis, and (ii) Cs⁺ sputtering beam (1 kV, 8 nA, 45°) for depth profiling. The

analytical and sputtered areas were maintained at $100 \times 100 \mu\text{m}^2$ and $300 \times 300 \mu\text{m}^2$ respectively. Chemical composition analysis was conducted on a Thermo Scientific ESCALAB250Xi XPS system. Ultraviolet photoelectron spectroscopy (UPS) measurement of perovskite films was performed by ESCALAB 250Xi spectrometer using a He I ($\hbar\nu = 21.22 \text{ eV}$) under -10 V bias, etched by Ar ion clusters. Photoluminescence characterization was performed using two complementary systems: Steady-state PL measurements employed a confocal Raman microscope (Princeton Instruments SP-2558) equipped with a 488 nm excitation laser (PicoQuant LDH-P-C-485, 0.4 mW, 1% OD filter) and PIXIS 100B_eXcelon CCD detector, analyzing $20 \times 20 \mu\text{m}^2$ regions. Time-resolved PL was acquired using a Metatest MStarter 100 system with picosecond laser excitation (488 nm, $\sim 2 \mu\text{m}$ spot radius) under ambient conditions. X-ray diffraction (XRD, Smartlab SE, Rigaku) was employed to examine the composition and crystalline structure of the samples, utilizing a Cu K α radiation source and a scan rate of 5° min^{-1} . Electroluminescence (EL) spectra were acquired using the Spectrum TEQ-EL electroluminescence quantum efficiency measurement system. The EL radiation flux was quantified by detecting emitted photons in all directions with an integrating sphere and calibrated spectrometers (Enlitech, LQE-50-PL). $J-V$ curves were recorded with a calibrated source-measure unit (Keithley 2420) under 1-sun illumination (Newport simulator, spectral mismatch $<2\%$). A mask of metal with no reflection with a 0.09 cm^2 aperture defined the device's active area. IPCE was recorded in ambient conditions across a wavelength range of 300 to 1200 nm (Saifan Photoelectric 7-SCSpec) using a dual Xenon/quartz halogen light source. The generated photocurrent was amplified and modulated via a lock-in amplifier, a certified silicon reference solar cell (Newport) was used for verifying the system prior to each test. Film morphology was analyzed using scanning electron microscopy (Hitachi SU8010) and atomic force microscopy (Bruker MULTIMODE 8). Surface electronic properties were evaluated by Kelvin probe force microscopy on the same AFM platform. Optical absorption properties were characterized by UV-vis-NIR spectroscopy (Shimadzu UV-3600 Plus).

ASSOCIATED CONTENT

Data Availability Statement

For access, please get in touch with the corresponding author.

Supporting Information

The Supporting Information is available free of charge at <https://pubs.acs.org/doi/10.1021/acsami.4c20406>.

Molecular Ball-and-Stick model of i-PAI; top-view AFM and SEM images of the control and i-PAI treated perovskite film; the UV-vis absorption spectra of the control and i-PAI treated perovskite film; Raman spectra of control and i-PAI treated perovskite film after 0 min, 10 and 20 min of 365 nm UV light exposure; XRD patterns of the control and i-PAI treated perovskite film; schematic diagram of lattice distortion; electroluminescence (EQE_{EL}) spectra for the normal structure devices; PL peak position mapping of control and i-PAI treated perovskite film after 0 min, 10 and 20 min of 365 nm UV light exposure; histogram of the PCE distribution for the control and i-PAI-treated wide-bandgap perovskite solar cells; Nyquist plots of devices measured in the dark conditions ([PDF](#))

AUTHOR INFORMATION

Corresponding Authors

Xing Li – Institute of Microelectronics of the Chinese Academy of Sciences, Beijing 100029, China; orcid.org/0000-0002-0794-3613; Email: lixing2021@ime.ac.cn

Guoping Gao – MOE Key Laboratory for Nonequilibrium Synthesis and Modulation of Condensed Matter, Shanxi Province Key Laboratory of Advanced Functional Materials and Mesoscopic Physics, Xi'an Jiaotong University, Xi'an, Shaanxi 710049, China; orcid.org/0000-0002-6106-7423; Email: guopinggao@xjtu.edu.cn

Molang Cai – New Energy School, North China Electric Power University, Beijing 102206, China; Beijing Key Laboratory of Novel Thin-Film Solar Cells, North China Electric Power University, Beijing 102206, China; orcid.org/0000-0001-8568-6897; Email: molangcai@ncepu.edu.cn

Authors

Xuzheng Feng – New Energy School, North China Electric Power University, Beijing 102206, China

Zhuoxin Li – New Energy School, North China Electric Power University, Beijing 102206, China

Yufei Xue – MOE Key Laboratory for Nonequilibrium Synthesis and Modulation of Condensed Matter, Shanxi Province Key Laboratory of Advanced Functional Materials and Mesoscopic Physics, Xi'an Jiaotong University, Xi'an, Shaanxi 710049, China

Xianggang Chen – New Energy School, North China Electric Power University, Beijing 102206, China

Xiaoxu Sun – New Energy School, North China Electric Power University, Beijing 102206, China

Jixiang Tang – New Energy School, North China Electric Power University, Beijing 102206, China; Institute of Microelectronics of the Chinese Academy of Sciences, Beijing 100029, China

Shuyi Liu – New Energy School, North China Electric Power University, Beijing 102206, China; orcid.org/0009-0005-7282-5962

Zishuo Wang – New Energy School, North China Electric Power University, Beijing 102206, China

Yuhang Xie – New Energy School, North China Electric Power University, Beijing 102206, China

Rui Jia – Institute of Microelectronics of the Chinese Academy of Sciences, Beijing 100029, China

Songyuan Dai – New Energy School, North China Electric Power University, Beijing 102206, China; Beijing Key Laboratory of Novel Thin-Film Solar Cells, North China Electric Power University, Beijing 102206, China; orcid.org/0000-0001-5710-9208

Complete contact information is available at:

<https://pubs.acs.org/10.1021/acsami.4c20406>

Author Contributions

M.C. and X.L. both the conceptualization and execution of this investigation. Sample preparation and device optimization of WBG perovskites were performed by X.F., with photophysical characterization executed by Z.L. using standardized protocols. G.G. and Y.X. conducted The DFT calculation. Z.L., S.L., and Z.W. performed device stability characterization of WBG PSCs. Manuscript preparation was jointly undertaken by Z.L. X.L., X.F., M.C., J.T., S.L., Z.W., and contributed to data analysis and experimental design. Everyone listed participated in manuscript editing.

Notes

The authors declare no competing financial interest.

ACKNOWLEDGMENTS

This work was sponsored by the National Natural Science Foundation of China (52202169, 22279033, and 12175305), Special Foundation for Carbon Peak Carbon Neutralization Technology Innovation Program of Jiangsu Province (BE2022026), the Project for Young Foreign Experts (QN2023124001L), the Fundamental Research Funds for the Central Universities (2021PT012), and the Beijing Nova Program (20230484298).

REFERENCES

- (1) Mariotti, S.; Köhnen, E.; Scheler, F.; Sveinbjörnsson, K.; Zimmerman, L.; Piot, M.; Yang, F.; Li, B.; Warby, J.; Musiienko, A.; Menzel, D.; Lang, F.; Keßler, S.; Levine, I.; Mantione, D.; Al-Ashouri, A.; Härtel, M. S.; Xu, K.; Cruz, A.; Kurpiers, J.; Wagner, P.; Köbler, H.; Li, J.; Magomedov, A.; Mecerreyes, D.; Unger, E.; Abate, A.; Stolterfoht, M.; Stannowski, B.; Schlatmann, R.; Korte, L.; Albrecht, S. Interface Engineering for High-Performance, Triple-Halide Perovskite–Silicon Tandem Solar Cells. *Science* **2023**, *381* (6653), 63–69.
- (2) Chin, X. Y.; Turkay, D.; Steele, J. A.; Tabean, S.; Eswara, S.; Mensi, M.; Fiala, P.; Wolff, C. M.; Paracchino, A.; Artuk, K.; Jacobs, D.; Guesnay, Q.; Sahli, F.; Andreatta, G.; Boccard, M.; Jeangros, Q.; Ballif, C. Interface Passivation for 31.25%-Efficient Perovskite/Silicon Tandem Solar Cells. *Science* **2023**, *381* (6653), 59–63.
- (3) Al-Ashouri, A.; Köhnen, E.; Li, B.; Magomedov, A.; Hempel, H.; Caprioglio, P.; Márquez, J. A.; Morales Vilches, A. B.; Kasparavicius, E.; Smith, J. A.; Phung, N.; Menzel, D.; Grischek, M.; Kegelmann, L.; Skroblin, D.; Gollwitzer, C.; Malinauskas, T.; Jošt, M.; Matič, G.; Rech, B.; Schlatmann, R.; Topič, M.; Korte, L.; Abate, A.; Stannowski, B.; Neher, D.; Stolterfoht, M.; Unold, T.; Getautis, V.; Albrecht, S. Monolithic Perovskite/Silicon Tandem Solar Cell with > 29% Efficiency by Enhanced Hole Extraction. *Science* **2020**, *370* (6522), 1300–1309.
- (4) Tockhorn, P.; Sutter, J.; Cruz, A.; Wagner, P.; Jäger, K.; Yoo, D.; Lang, F.; Grischek, M.; Li, B.; Li, J.; Shargaiava, O.; Unger, E.; Al-Ashouri, A.; Köhnen, E.; Stolterfoht, M.; Neher, D.; Schlatmann, R.; Rech, B.; Stannowski, B.; Albrecht, S.; Becker, C. Nano-Optical Designs for High-Efficiency Monolithic Perovskite–Silicon Tandem Solar Cells. *Nat. Nanotechnol.* **2022**, *17* (11), 1214–1221.
- (5) Stranks, S. D.; Eperon, G. E.; Grancini, G.; Menelaou, C.; Alcocer, M. J. P.; Leijtens, T.; Herz, L. M.; Petrozza, A.; Snaith, H. J. Electron-Hole Diffusion Lengths Exceeding 1 Micrometer in an Organometal Trihalide Perovskite Absorber. *Science* **2013**, *342* (6156), 341–344.
- (6) Wehrenfennig, C.; Eperon, G. E.; Johnston, M. B.; Snaith, H. J.; Herz, L. M. High Charge Carrier Mobilities and Lifetimes in Organoolead Trihalide Perovskites. *Adv. Mater.* **2014**, *26* (10), 1584–1589.
- (7) Zhao, Y.; Ma, F.; Qu, Z.; Yu, S.; Shen, T.; Deng, H.-X.; Chu, X.; Peng, X.; Yuan, Y.; Zhang, X.; You, J. Inactive $(\text{PbI}_2)_2\text{RbCl}$ Stabilizes Perovskite Films for Efficient Solar Cells. *Science* **2022**, *377* (6605), 531–534.
- (8) Xing, G.; Mathews, N.; Sun, S.; Lim, S. S.; Lam, Y. M.; Grätzel, M.; Mhaisalkar, S.; Sum, T. C. Long-Range Balanced Electron- and Hole-Transport Lengths in Organic-Inorganic $\text{CH}_3\text{NH}_3\text{PbI}_3$. *Science* **2013**, *342* (6156), 344–347.
- (9) Zhang, S.; Ye, F.; Wang, X.; Chen, R.; Zhang, H.; Zhan, L.; Jiang, X.; Li, Y.; Ji, X.; Liu, S.; Yu, M.; Yu, F.; Zhang, Y.; Wu, R.; Liu, Z.; Ning, Z.; Neher, D.; Han, L.; Lin, Y.; Tian, H.; Chen, W.; Stolterfoht, M.; Zhang, L.; Zhu, W.-H.; Wu, Y. Minimizing Buried Interfacial Defects for Efficient Inverted Perovskite Solar Cells. *Science* **2023**, *380* (6643), 404–409.
- (10) Mo, Y.; Wang, C.; Zheng, X.; Zhou, P.; Li, J.; Yu, X.; Yang, K.; Deng, X.; Park, H.; Huang, F.; Cheng, Y. Nitrogen-doped Tin Oxide Electron Transport Layer for Stable Perovskite Solar Cells with Efficiency over 23%. *Interdiscip. Mater.* **2022**, *1* (2), 309–315.
- (11) Lee, J.-W.; Tan, S.; Seok, S. I.; Yang, Y.; Park, N.-G. Rethinking the A Cation in Halide Perovskites. *Science* **2022**, *375* (6583), No. eabj1186.
- (12) Green, M. A.; Ho-Baillie, A.; Snaith, H. J. The Emergence of Perovskite Solar Cells. *Nat. Photonics* **2014**, *8* (7), 506–514.
- (13) Li, Z.; Li, X.; Chen, X.; Cui, X.; Guo, C.; Feng, X.; Ren, D.; Mo, Y.; Yang, M.; Huang, H.; Jia, R.; Liu, X.; Han, L.; Dai, S.; Cai, M. In Situ Epitaxial Growth of Blocking Structure in Mixed-Halide Wide-Band-Gap Perovskites for Efficient Photovoltaics. *Joule* **2023**, *7* (6), 1363–1381.
- (14) Xu, Z.; Kerner, R. A.; Berry, J. J.; Rand, B. P. Iodine Electrochemistry Dictates Voltage-Induced Halide Segregation Thresholds in Mixed-Halide Perovskite Devices. *Adv. Funct. Mater.* **2022**, *32* (33), No. 2203432.
- (15) Phung, N.; Mattoni, A.; Smith, J. A.; Skroblin, D.; Köbler, H.; Choubrac, L.; Breternitz, J.; Li, J.; Unold, T.; Schorr, S.; Gollwitzer, C.; Scheblykin, I. G.; Unger, E. L.; Saliba, M.; Meloni, S.; Abate, A.; Merdasa, A. Photoprotection in Metal Halide Perovskites by Ionic Defect Formation. *Joule* **2022**, *6* (9), 2152–2174.
- (16) Cui, Z.; Zhang, Q.; Bai, Y.; Chen, Q. Issues of Phase Segregation in Wide-Bandgap Perovskites. *Mater. Chem. Front.* **2023**, *7* (10), 1896–1911.
- (17) Wang, Z.; Zeng, L.; Zhu, T.; Chen, H.; Chen, B.; Kubicki, D. J.; Balvanz, A.; Li, C.; Maxwell, A.; Ugur, E.; Dos Reis, R.; Cheng, M.; Yang, G.; Subedi, B.; Luo, D.; Hu, J.; Wang, J.; Teale, S.; Mahesh, S.; Wang, S.; Hu, S.; Jung, E. D.; Wei, M.; Park, S. M.; Grater, L.; Aydin, E.; Song, Z.; Podraza, N. J.; Lu, Z.-H.; Huang, J.; Dravid, V. P.; De Wolf, S.; Yan, Y.; Grätzel, M.; Kanatzidis, M. G.; Sargent, E. H. Suppressed Phase Segregation for Triple-Junction Perovskite Solar Cells. *Nature* **2023**, *618* (7963), 74–79.
- (18) Singh, S.; Siliavka, E.; Löffler, M.; Vaynzof, Y. Impact of Buried Interface Texture on Compositional Stratification and Ion Migration in Perovskite Solar Cells. *Adv. Funct. Mater.* **2024**, *34*, No. 2402655.
- (19) Zhong, Y.; Yang, J.; Wang, X.; Liu, Y.; Cai, Q.; Tan, L.; Chen, Y. Inhibition of Ion Migration for Highly Efficient and Stable Perovskite Solar Cells. *Adv. Mater.* **2023**, *35* (52), No. 2302552.
- (20) Walsh, A.; Stranks, S. D. Taking Control of Ion Transport in Halide Perovskite Solar Cells. *ACS Energy Lett.* **2018**, *3* (8), 1983–1990.
- (21) Yi, H. T.; Rangan, S.; Tang, B.; Frisbie, C. D.; Bartynski, R. A.; Gartstein, Y. N.; Podzorov, V. Electric-Field Effect on Photoluminescence of Lead-Halide Perovskites. *Mater. Today* **2019**, *28*, 31–39.
- (22) Chen, J.; Ge, K.; Chen, B.; Guo, J.; Yang, L.; Wu, Y.; Coletti, G.; Liu, H.; Li, F.; Liu, D.; Wang, Z.; Xu, Y.; Mai, Y. Establishment of a Novel Functional Group Passivation System for the Surface Engineering of C-Si Solar Cells. *Sol. Energy Mater. Sol. Cells* **2019**, *195*, 99–105.
- (23) Glunz, S. W.; Biro, D.; Rein, S.; Warta, W. Field-Effect Passivation of the SiO_2Si Interface. *J. Appl. Phys.* **1999**, *86* (1), 683–691.
- (24) Dingemans, G.; Terlinden, N. M.; Pierreux, D.; Profijt, H. B. Influence of the Oxidant on the Chemical and Field-Effect Passivation of Si by ALD Al_2O_3 . *Electrochim. Solid-State Lett.* **2011**, *14*, No. H1, DOI: [10.1149/1.3501970](https://doi.org/10.1149/1.3501970).
- (25) Ma, Y.; Gong, J.; Zeng, P.; Liu, M. Recent Progress in Interfacial Dipole Engineering for Perovskite Solar Cells. *Nano-Micro Lett.* **2023**, *15* (1), No. 173.
- (26) Chen, H.; Maxwell, A.; Li, C.; Teale, S.; Chen, B.; Zhu, T.; Ugur, E.; Harrison, G.; Grater, L.; Wang, J.; Wang, Z.; Zeng, L.; Park, S. M.; Chen, L.; Serles, P.; Awani, R. A.; Subedi, B.; Zheng, X.; Xiao, C.; Podraza, N. J.; Filteeter, T.; Liu, C.; Yang, Y.; Luther, J. M.; De Wolf, S.; Kanatzidis, M. G.; Yan, Y.; Sargent, E. H. Regulating Surface Potential Maximizes Voltage in All-Perovskite Tandems. *Nature* **2023**, *613* (7945), 676–681.
- (27) Liu, C.; Yang, Y.; Chen, H.; Xu, J.; Liu, A.; Bati, A. S. R.; Zhu, H.; Grater, L.; Hadke, S. S.; Huang, C.; Sangwan, V. K.; Cai, T.; Shin, D.; Chen, L. X.; Hersam, M. C.; Mirkin, C. A.; Chen, B.; Kanatzidis, M. G.; Sargent, E. H. Bimolecularly Passivated Interface Enables

- Efficient and Stable Inverted Perovskite Solar Cells. *Science* **2023**, *382* (6672), 810–815.
- (28) Yang, Y.; Chen, H.; Liu, C.; Xu, J.; Huang, C.; Malliakas, C. D.; Wan, H.; Bati, A. S. R.; Wang, Z.; Reynolds, R. P.; Gilley, I. W.; Kitade, S.; Wiggins, T. E.; Zeiske, S.; Suragtchuu, S.; Batmunkh, M.; Chen, L. X.; Chen, B.; Kanatzidis, M. G.; Sargent, E. H. Amidination of Ligands for Chemical and Field-Effect Passivation Stabilizes Perovskite Solar Cells. *Science* **2024**, *386* (6724), 898–902.
- (29) Cai, M.; Ishida, N.; Li, X.; Yang, X.; Noda, T.; Wu, Y.; Xie, F.; Naito, H.; Fujita, D.; Han, L. Control of Electrical Potential Distribution for High-Performance Perovskite Solar Cells. *Joule* **2018**, *2* (2), 296–306.
- (30) Wu, Y.; Chang, B.; Wang, L.; Li, H.; Pan, L.; Liu, Z.; Yin, L. Intrinsic Dipole Arrangement to Coordinate Energy Levels for Efficient and Stable Perovskite Solar Cells. *Adv. Mater.* **2023**, *35* (18), No. 2300174.
- (31) Zheng, X.; Li, Z.; Zhang, Y.; Chen, M.; Liu, T.; Xiao, C.; Gao, D.; Patel, J. B.; Kuciauskas, D.; Magomedov, A.; Scheidt, R. A.; Wang, X.; Harvey, S. P.; Dai, Z.; Zhang, C.; Morales, D.; Pruett, H.; Wieliczka, B. M.; Kirmani, A. R.; Padture, N. P.; Graham, K. R.; Yan, Y.; Nazeeruddin, M. K.; McGehee, M. D.; Zhu, Z.; Luther, J. M. Co-Deposition of Hole-Selective Contact and Absorber for Improving the Processability of Perovskite Solar Cells. *Nat. Energy* **2023**, *8* (5), 462–472.
- (32) Zheng, X.; Li, Z.; Zhang, Y.; Chen, M.; Liu, T.; Xiao, C.; Gao, D.; Patel, J. B.; Kuciauskas, D.; Magomedov, A.; Scheidt, R. A.; Wang, X.; Harvey, S. P.; Dai, Z.; Zhang, C.; Morales, D.; Pruett, H.; Wieliczka, B. M.; Kirmani, A. R.; Padture, N. P.; Graham, K. R.; Yan, Y.; Nazeeruddin, M. K.; McGehee, M. D.; Zhu, Z.; Luther, J. M. Co-Deposition of Hole-Selective Contact and Absorber for Improving the Processability of Perovskite Solar Cells. *Nat. Energy* **2023**, *8* (5), 462–472.
- (33) Li, C.; Zhang, N.; Gao, P. Lessons Learned: How to Report XPS Data Incorrectly about Lead-Halide Perovskites. *Mater. Chem. Front.* **2023**, *7* (18), 3797–3802.
- (34) Li, Z.; Li, X.; Wang, M.; Cai, M.; Shi, X.; Mo, Y.; Chen, X.; Ren, D.; Yang, M.; Liu, X.; Jia, R.; Medhekar, N. V.; Dai, S. Enhanced Photovoltaic Performance via a Bifunctional Additive in Tin-Based Perovskite Solar Cells. *ACS Appl. Energy Mater.* **2022**, *5* (1), 108–115.
- (35) Zheng, X.; Liu, J.; Liu, T.; Aydin, E.; Chen, M.; Yan, W.; De Bastiani, M.; Allen, T. G.; Yuan, S.; Kirmani, A. R.; Baustert, K. N.; Salvador, M. F.; Turedi, B.; Alsalloum, A. Y.; Almasabi, K.; Kotsov, K.; Gereige, I.; Liao, L.-S.; Luther, J. M.; Graham, K. R.; Mohammed, O. F.; De Wolf, S.; Bakr, O. M. Photoactivated P-Doping of Organic Interlayer Enables Efficient Perovskite/Silicon Tandem Solar Cells. *ACS Energy Lett.* **2022**, *7* (6), 1987–1993.
- (36) Chen, X.; Kamat, P. V.; Janáky, C.; Samu, G. F. Charge Transfer Kinetics in Halide Perovskites: On the Constraints of Time-Resolved Spectroscopy Measurements. *ACS Energy Lett.* **2024**, *9* (6), 3187–3203.
- (37) Ma, Y.; Zeng, C.; Zeng, P.; Hu, Y.; Li, F.; Zheng, Z.; Qin, M.; Lu, X.; Liu, M. How Do Surface Polar Molecules Contribute to High Open-Circuit Voltage in Perovskite Solar Cells? *Adv. Sci.* **2023**, *10* (17), No. 2205072.
- (38) Garai, R.; Sharma, B.; Afroz, M. A.; Choudhary, S.; Sharma, T.; Metcalf, I.; Tailor, N. K.; Iyer, P. K.; Mohite, A. D.; Satapathi, S. High-Efficiency Semitransparent Perovskite Solar Cells Enabled by Controlling the Crystallization of Ultrathin Films. *ACS Energy Lett.* **2024**, *9* (6), 2936–2943.
- (39) Wang, L.; Song, Q.; Pei, F.; Chen, Y.; Dou, J.; Wang, H.; Shi, C.; Zhang, X.; Fan, R.; Zhou, W.; Qiu, Z.; Kang, J.; Wang, X.; Lambertz, A.; Sun, M.; Niu, X.; Ma, Y.; Zhu, C.; Zhou, H.; Hong, J.; Bai, Y.; Duan, W.; Ding, K.; Chen, Q. Strain Modulation for Light-Stable n-i-p Perovskite/Silicon Tandem Solar Cells. *Adv. Mater.* **2022**, *34* (26), No. 2201315.
- (40) Sidhik, S.; Metcalf, I.; Li, W.; Kodalle, T.; Dolan, C. J.; Khalili, M.; Hou, J.; Mandani, F.; Torma, A.; Zhang, H.; Garai, R.; Persaud, J.; Marciel, A.; Puente, I. A. M.; Reddy, G. N. M.; Balvanz, A.; Alam, M.; Katan, C.; Tsai, E.; Ginger, D.; Fenning, D. P.; Kanatzidis, M. G.; Sutter-Fella, C. M.; Even, J.; Mohite, A. D. Two-Dimensional Perovskite Templates for Durable, Efficient Formamidinium Perovskite Solar Cells. *Science* **2024**, *384* (6701), 1227–1235.
- (41) Li, X.; Li, K.; Wang, B.; Zhang, X.; Yue, S.; Li, Y.; Chen, Q.; Li, S.; Yue, T.; Zhou, H.; Zhang, Y. Efficient and Stable Quasi-2D Perovskite Solar Cells Enabled by Thermal-Aged Precursor Solution. *Adv. Funct. Mater.* **2021**, *31* (52), No. 2107675.
- (42) Yang, Y.; Chen, R.; Wu, J.; Dai, Z.; Luo, C.; Fang, Z.; Wan, S.; Chao, L.; Liu, Z.; Wang, H. Bilateral Chemical Linking at NiOx Buried Interface Enables Efficient and Stable Inverted Perovskite Solar Cells and Modules. *Angew. Chem. Int. Ed.* **2024**, *63*, No. e202409689.

The image shows the homepage of CAS Insights, a service from the American Chemical Society. The page is filled with various news articles and features. At the top, there's a banner for 'CAS Insights™' with the tagline 'Accelerating your scientific perspective at the intersection of science, technology, and innovation'. Below the banner, there are several news cards. One card on the left discusses 'How to report XPS data correctly about lead-halide perovskites'. Another card in the center talks about 'Webinar: Emerging areas in biomaterials - Reshaping medicine and human health'. To the right, there's a card about 'Graphene - advancing new applications on the promise of graphene'. The overall layout is clean and modern, designed to keep users updated on the latest scientific developments.

CAS INSIGHTS™

EXPLORE THE INNOVATIONS SHAPING TOMORROW

Discover the latest scientific research and trends with CAS Insights. Subscribe for email updates on new articles, reports, and webinars at the intersection of science and innovation.

Subscribe today

CAS
A division of the
American Chemical Society